Inferring Maps of Forces inside Cell Membrane Microdomains

J.-B. Masson,[1,*] D. Casanova,[2] S. Türkcan,[2] G. Voisinne,[1] M. R. Popoff,[3] M. Vergassola,[1] and A. Alexandrou[2]

[1]*Institut Pasteur, CNRS URA 2171, Unit In Silico Genetics, 75724 Paris Cedex 15, France*

[2]*Laboratoire d'Optique et Biosciences, Ecole Polytechnique, CNRS, INSERM, 91128 Palaiseau, France*

[3]*Institut Pasteur, Bactéries anaérobies et Toxines, 75724 Paris Cedex 15, France*

(Received 9 September 2008; published 29 January 2009)

Mapping of the forces on biomolecules in cell membranes has spurred the development of effective labels, e.g., organic fluorophores and nanoparticles, to track trajectories of single biomolecules. Standard methods use particular statistics, namely the mean square displacement, to analyze the underlying dynamics. Here, we introduce general inference methods to fully exploit information in the experimental trajectories, providing sharp estimates of the forces and the diffusion coefficients in membrane microdomains. Rapid and reliable convergence of the inference scheme is demonstrated on trajectories generated numerically. The method is then applied to infer forces and potentials acting on the receptor of the ϵ toxin labeled by lanthanide-ion nanoparticles. Our scheme is applicable to any labeled biomolecule and results show its general relevance for membrane compartmentation.

DOI: 10.1103/PhysRevLett.102.048103 PACS numbers: 87.80.Nj, 02.50.Tt, 05.10.Gg, 87.16.dp

The motion of proteins and lipids in cell membranes and its relation to biological function have attracted considerable interest in recent years [1]. Motion is commonly followed by tracking of single biomolecules labeled by an organic fluorophore or an inorganic nanoparticle that allows detection via fluorescence, light scattering, etc. [2]. Trajectories are usually analyzed by plotting the mean-square displacement (MSD) as a function of time. Parameters like diffusion coefficients and domain sizes are extracted by fitting MSD curves to analytical behaviors expected for different modes of motion, e.g., free Brownian diffusion, directed, confined or anomalous motion [2].

A major physical motivation to biomolecule tracking stems from the actively debated origin of membrane compartmentation. Free diffusion of membrane proteins in a sea of lipids was first postulated in the fluid mosaic model [3]. Following experimental observations of confinement, the lipid rafts [4] and the picket and fence [5] models were proposed. In the former, membrane proteins are preferentially located in domains with different lipid composition (lipid rafts). In the latter, compartmentation is ascribed to the combined action of the cytoskeleton and anchored transmembrane proteins, forming fences and pickets, respectively. Alternative models relying on more specific mechanisms of protein-protein interactions have also been proposed [6,7]. Additional complexity arises from the fact that different confinement mechanisms may coexist and depend on the type of biomolecule [8].

The MSD-based approach has been used extensively. Alternative observables related to first-passage times [9] or radial particle density distribution [10] have been proposed recently. More information on the dynamics is hidden in the full trajectory of biomolecules, though. Focusing on a single observable, e.g., the second-order moment for MSD, has the virtue of simplicity yet it wipes out information. In particular, it makes harder discriminating among different models of motion and does not provide systematic assessment of their validity. A more general approach based on inference methods [11] is taken by considering the likelihoods of the models themselves. A quantitative sense of their validity is thus obtained, together with systematic estimates of the parameters of the models and their uncertainties.

Our aim here is to present a general inference approach to obtain maps of the forces and the potentials involved in the confined motion of biomolecules in cell membranes. Inferences are shown to provide sharp estimations of the local forces acting in the microdomains. We specifically consider the case of the receptors of ϵ toxin in the membrane of Madin-Darby canine kidney (MDCK) cells.

The ϵ toxin is responsible for lethal enterotoxemia in livestock, due to the Gram-positive bacterium *Clostridium perfringens* (types *B* and *D*). A relatively inactive peptidic prototoxin is first synthesized and is then converted to a highly potent mature protein by cleavage and removal of terminal amino acids. The mature protein targets a specific receptor located preferentially in detergent-resistant domains of MDCK cells [12]. The protein acts by heptamerizing, which leads to the formation of pores and the rapid modification of the membrane permeability to ions, causing cell death without any entry of the toxin into the cytosol [13,14].

To label the ϵ toxin, we used 30–50 nm amine-coated lanthanide oxide nanoparticles (NPs) $Y_{0.6}Eu_{0.4}VO_4$ (mean toxin:NP ratio, 1:1; see [15]). These nanoparticles present several advantages: they are highly photostable without emission intermittency, they are synthesized directly in water and present extremely narrow emission, allowing efficient rejection of cell fluorescence [16]. Their size is directly determined from their luminosity [17]. Different emission colors are obtained using different lanthanide ions [18].

 © 2009 The American Physical Society

We used a wide-field inverted microscope (Zeiss Axiovert 100) equipped with a 63×, NA = 1.4 oil-immersion objective and an EM-CCD (Roper Scientific QuantEM:512SC). The Eu^{3+} ions of the nanoparticles were excited with the 465.8-nm line of an Ar^{+}-ion laser and their emission was detected using a 617/8M filter (Chroma). MDCK cells were grown to confluency on glass coverslips. They were then rinsed, incubated with 0.04 nM of labeled ϵ toxin or prototoxins for 20 min, rinsed 3 times, and observed in Hanks buffer containing 1% fetal calf serum and 1% penicillin-streptomycin either at 20 or 30 °C.

In all experiments (~400 cells), we observed several nanoparticles bound to a specific receptor on the cell membrane. We verified specificity of binding by preincubating the toxin for 1 h with an ϵ toxin antibody that prevents binding to the membrane (obtained as in [13]) and verifying the absence of nanoparticles bound to the cells. Toxins were kept at concentrations low enough to ensure that single toxins (and not oligomers) are tracked. Trajectories similar to those of prototoxins, which do not oligomerize, were indeed observed. The mean toxin:NP ratio 1:1 implies, assuming a Poisson distribution, that the fraction of NPs bound to zero, one and two or more toxins are 37%, 37%, and 26%, respectively. Nanoparticles without toxins do not bind to the cells and are rinsed away. Given the size of the NPs, it is improbable that more than one toxin is present on the same area of the NP surface allowing simultaneous binding to more than one receptor. Furthermore, the binding ability of a fraction of the toxins may be impaired by the coupling to the NPs. We therefore estimate that the fraction of NPs bound to more than one receptor is less than 10%. We also labeled ϵ toxin with the organic fluorophore Cy3 and observed again similar trajectories. This implies that the nanoparticle label does not modify the receptor motion, which is thus determined by the receptor mass and the membrane characteristics (viscosity, forces, etc.). The receptor motion was studied during 150 to 300 s. Figure 1 shows a portion of the confined trajectory of a prototoxin bound to its receptor. We verified that, given the diffusion coefficient and the domain size, we are not limited by the image acquisition time (21.4 or 51.4 ms) [19,20]. Relatively short portions of trajectories were considered, so as to exclude possible drifting of the membrane domain, the cell, or the microscope setup.

Langevin equations for the position $\boldsymbol{r}(t)$ and the velocity $\boldsymbol{v}(t)$ of a biomolecule subject to molecular diffusion and to the force induced by a potential V (see Fig. 2) are

$$\frac{d\boldsymbol{r}}{dt} = \boldsymbol{v}; \qquad m\frac{d\boldsymbol{v}}{dt} = -\gamma\boldsymbol{v} - \nabla V(\boldsymbol{r}) + \sqrt{2D\gamma^2}\boldsymbol{\xi}. \quad (1)$$

Here, m is the mass of the biomolecule, γ and D are the friction and the diffusion coefficients inside the microdomain of the membrane. The zero-average Gaussian noise $\boldsymbol{\xi}(t)$ rapidly fluctuates in time, accounting for the effect of thermal noise. Smoluchowski's overdamped approximation [21] to (1) is sufficient for the motion of biomolecules. Indeed, the typical time for the relaxation of the velocity to local equilibrium is $\tau = \frac{m}{\gamma} \simeq 10^{-16}$ s (since $m \simeq 10^{-22}$ kg and $\gamma \simeq 10^{-6}$ kg/s [22]). Hence, the velocity is slaved to its local forcing and (1) reduces to

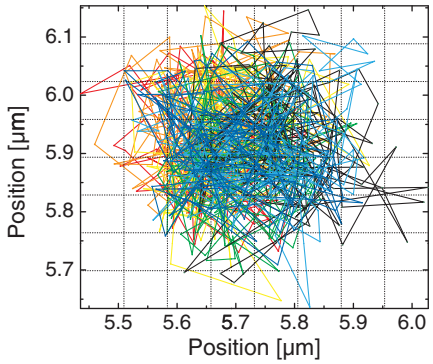


FIG. 1 (color). A 60-s trajectory of a $Y_{0.6}Eu_{0.4}VO_4$ nanoparticle labeling ϵ prototoxin bound to its receptor on the membrane of an MDCK cell. The line color changes from red to blue (beginning/end of the trajectory). The motion is clearly confined. See Ref. [25] for a movie at real speed (scale bar: 1 μm). Excitation intensity, 0.2 kW/cm^2; integration time, 50 ms; readout time, 1.4 ms; r localization precision, 20 nm; temperature, 20 °C. Inferred forces and potentials are shown in Fig. 2(a). The dashed lines indicate the mesh squares used for the inference.

$$\frac{d\boldsymbol{r}}{dt} = -\frac{\nabla V(\boldsymbol{r})}{\gamma} + \sqrt{2D}\boldsymbol{\xi}. \quad (2)$$

The Fokker-Planck equation [23] associated to (2) reads

$$\partial_t P = -\tfrac{1}{\gamma}\boldsymbol{\nabla}\cdot(\boldsymbol{F}P) + D\Delta P, \quad (3)$$

where the force $\boldsymbol{F} \equiv -\boldsymbol{\nabla}V$. Kolmogorov equation (3) governs the transition probability $P(\boldsymbol{r}, t|\boldsymbol{r}_0, t_0)$ to get to the space-time point $(\boldsymbol{r}, t)$ conditional to the initial space-time position $(\boldsymbol{r}_0, t_0)$ of the biomolecule. It follows from (3) that the probability P can be expressed as a path integral [24] over all paths $\boldsymbol{r}(s)$ connecting $\boldsymbol{r}_0$ to $\boldsymbol{r}$:

$$P(\boldsymbol{r}, t|\boldsymbol{r}_0, t_0) \propto \int \mathcal{D}\boldsymbol{r}(s) e^{-\int ds Q(\boldsymbol{r}(s))}. \quad (4)$$

The term $Q(\boldsymbol{r}(s)) \equiv (d\boldsymbol{r}(s)/ds - \boldsymbol{F}(\boldsymbol{r}(s))/\gamma)^2/4D$ is the quadratic Gaussian weight governing the probability of displacements over an infinitesimal time interval.

In practice, space is discretized in a fine regular mesh of n^2 squares, as shown in Fig. 1 ($n = 8$). The size of the mesh is taken small enough for the forces to be smooth on that scale. At the lowest order, forces are approximated by a constant value within each mesh square and we shall show later that higher-order variations are indeed negligible. The integral appearing at the exponential in (4) is approximated by the corresponding discrete Riemann sum [see (6)]. Mesh squares $\mathcal{S}_{i,j}$ are indexed by the pair (i, j) (with $i, j = 1, \ldots, n$) and the force acting in $\mathcal{S}_{i,j}$ is denoted $\boldsymbol{F}_{i,j}$. Our goal is to estimate the $2n^2 + 1$ unknowns

$U = \{D, \{\boldsymbol{F}_{i,j}\}\}$, i.e., the forces and the diffusivity within a membrane subdomain, governing the trajectories of the labeled biomolecule. Variations in D can be handled similarly (see below).

Inference methods (see, e.g., [11]) generally feature two steps: (a) the derivation of the *posterior* probability distribution of the unknown parameters of the model given the experimental observations; (b) sampling from the *posterior* distribution to estimate the parameters. Specifically, it follows from Bayes rule that the *posterior* probability distribution $P(U|T)$ of the set of unknown parameters U given an observed trajectory T reads

$$P(U|T) = \frac{P(T|U)P_0(U)}{P(T)}, \tag{5}$$

where $P(T|U)$ is the likelihood of a trajectory given the parameters U and $P(T)$ is a normalizing constant. $P_0(U)$ is the *prior* probability, which we take constant. As for the sampling part (b), we used Monte Carlo methods to compute the average over the *posterior* distributions. The latter are generally well peaked and maximum values provide then good estimates of the average values.

An asset of our specific problem is that the diffusivity D is the only global parameter while the n^2 forces $\boldsymbol{F}_{i,j}$ appear in the likelihood additively at the exponential. It follows that the contributions of the various squares of the mesh factorize as $P(U|T) = \prod_{i,j=1}^{n} P(\boldsymbol{F}_{i,j}, D|T)$. The contribution of each mesh square reads

$$P(\boldsymbol{F}_{i,j}, D|T) \propto \prod_{\mu:\boldsymbol{r}_\mu \in \mathcal{S}_{i,j}} \frac{\exp\left[-\frac{(\boldsymbol{r}_{\mu+1}-\boldsymbol{r}_\mu-\boldsymbol{F}_{i,j}\Delta t/\gamma)^2}{4D\Delta t}\right]}{4\pi D\Delta t}. \tag{6}$$

Here, μ indexes the various time steps (discretized by Δt) and the product is restricted to those times when the biomolecule is detected within the mesh square $\mathcal{S}_{i,j}$. Note that discretization introduces *a fortiori* an ambiguity when the biomolecule crosses the lines of the mesh and moves to a new square. The choice made in (6) is to simply use indices of the starting square. Corrections will be shown shortly to be negligible.

The crucial element ensuring well-peaked *posterior* distributions and sharp inferences is that the trajectories of the biomolecules are well confined to subdomains. It follows that the various squares of the mesh are crossed multiple times, permitting the acquisition of a massive amount of information. Even for those squares where the largest forces are measured, i.e., the residence time is the shortest, the amount of data is sufficient to permit sharp inferences. Note also that *posterior* distributions for the forces are Gaussian, as seen directly in (6).

To have a quantitative sense of the quality of the inference scheme, we numerically generated ensembles of trajectories with the same force fields and diffusion coefficients as obtained from the experimental data. *Posterior* distributions were found to be sharply peaked at the values used to generate the trajectories. Typical evolutions of inferred values vs the number of points used for the inference are shown in Fig. 3. Convergence is manifestly rapid and the standard deviation brackets the real value even for few data points, providing a sensible estimate of the error bars. Predictions by our method were found to be more precise and to require less data points than those based on a single statistic, e.g., MSD or radial particle density distribution. In summary, simulations provide strong support to the validity of the inference method.

To visualize the results, it is convenient to plot the potentials V as in Fig. 2. To that purpose, the potential is written as a polynomial of order C ($C = 4$ in Fig. 2): $V(\boldsymbol{r}) = \sum_{j=0}^{C}\sum_{i=0}^{j} \alpha_{ij} x^i y^{j-i}$. The constants α_{ij} are fitted to the experimental force fields, minimizing the squared

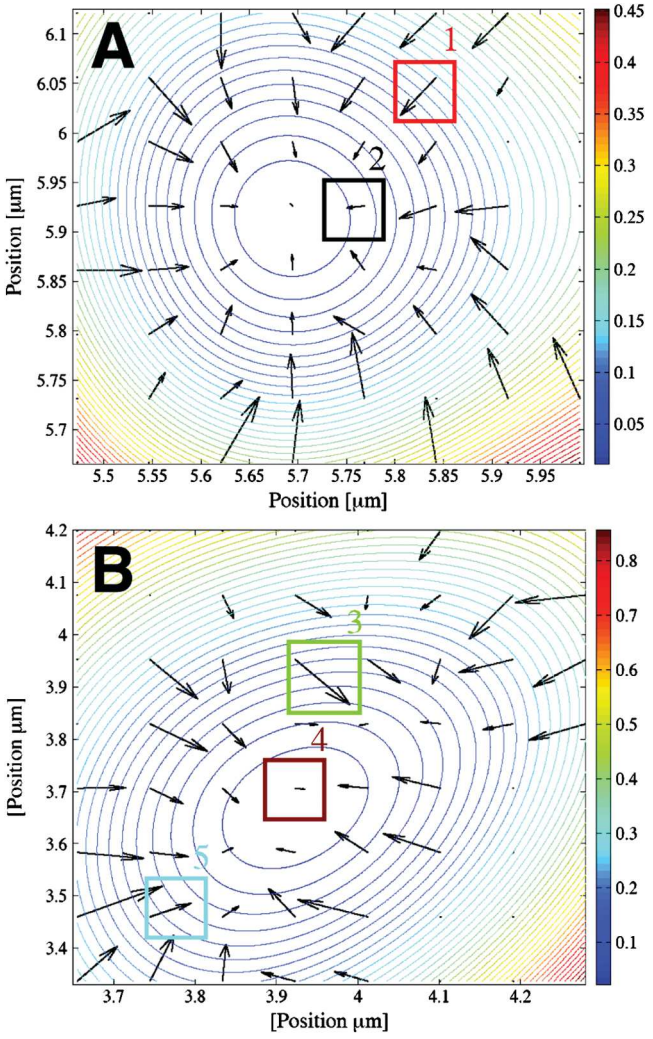


FIG. 2 (color). Force and potential fields inferred inside two membrane microdomains. The length of the arrows is proportional to the magnitude of the force. The potential is plotted as level curves with the bar indicating the potential's amplitude on the isoline. The interpolation scheme described in the text was used, leading to an effective time step of 5 ms. The diffusion coefficent for (a) is 4.75×10^{-2} $\mu m^2 s^{-1}$ and for (b) is 8.15×10^{-2} $\mu m^2 s^{-1}$. Posterior distributions for the five locations indicated by the squares are shown in Fig. 4.

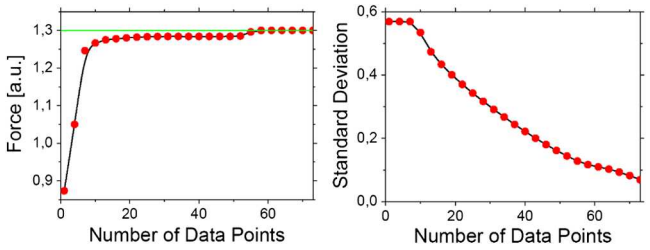


FIG. 3 (color online). Typical evolution of the inferred value of a local force (left) and its standard deviation (right) with the number of points used to infer them. Note the rapid convergence to the real value of the force (indicated by the solid horizontal line).

error by standard simplex methods. Potentials that we find are incompatible with a cytoskeleton fence-type model, where a steep wall-like potential is expected. This type of domain, however, may still influence the receptor trajectories on time scales below our resolution. Variations within microdomains for the diffusivities were found to be small, i.e., about 4% vs 65% for the forces.

Discretization errors were controlled by the following method. Given two acquisitions $(\boldsymbol{x}_1, t_1)$ and $(\boldsymbol{x}_2, t_2 = t_1 + \Delta t)$, we interpolate their transition probability by summing over all possible positions $\boldsymbol{x}'$ at the intermediate time $t' = t_1 + \Delta t/2$, i.e., $P(x_2, t_2|x_1, t_1) = \int dx' P(x_2, t_2|x', t')P(x', t'|x_1, t_1)$. The process can be further refined by introducing additional intermediate points. The effect of the interpolation mostly amounts to a reduction of the error bars, without any major shift in the estimates of the forces, as can be seen in Fig. 4.

In conclusion, we have developed an inference approach that fully exploits information hidden in labeled biomolecule trajectories. The technique is generally applicable to any type of biomolecule and trajectory, including intermittent trajectories like those obtained with blinking quantum dots, and for forces and domains that change in time. We have explicitly demonstrated the value of the method by mapping the forces and the potentials involved in the confined motion of the ϵ toxin receptor in the membrane of MDCK cells. Results obtained here indicate that the method, especially in combination with data on cytoskeleton destruction and cholesterol depletion, is poised to shed light onto the controversial mechanisms of membrane compartmentation.

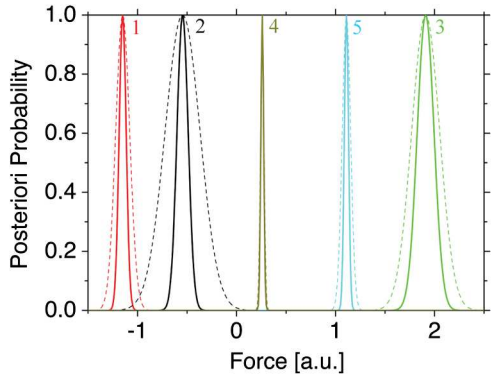


FIG. 4 (color online). Posterior probability distributions of the forces at the locations indicated with the squares in Fig. 2. The curves for horizontal (vertical) components of the force are 2,4,5 (1,3). Solid curves are obtained by the interpolation scheme described in the text. Note that average values are extremely close to those obtained without interpolation (dashed curves) yet the variance is reduced.

We are grateful to G. Mialon, T. Gacoin, and J.-P. Boilot for the amine-coated nanoparticles, to C. Bouzigues for helpful discussions, to the Region Ile-de-France Nanosciences Competence Center, the Fonds National de la Science (ACI DRAB), the ANR PNANO (Grant 062 03), and the Delegation Generale de l'Armement (D. C.) for financial support.

*Corresponding author.
jbmasson@pasteur.fr

[1] M. J. Saxton, Nat. Methods **5**, 671 (2008).
[2] M. J. Saxton and K. Jacobson, Annu. Rev. Biophys. Biomol. Struct. **26**, 373 (1997).
[3] S. J. Singer and G. L. Nicolson, Science **175**, 720 (1972).
[4] K. Simons and E. Ikonen, Nature (London) **387**, 569 (1997).
[5] A. Kusumi *et al.*, Annu. Rev. Biophys. Biomol. Struct. **34**, 351 (2005).
[6] F. Daumas *et al.*, Biophys. J. **84**, 356 (2003).
[7] J. J. Sieber *et al.*, Science **317**, 1072 (2007).
[8] P.-F. Lenne *et al.*, EMBO J. **25**, 3245 (2006).
[9] S. Condamin *et al.*, Proc. Natl. Acad. Sci. U.S.A. **105**, 5675 (2008).
[10] S. Jin *et al.*, Biophys. J. **93**, 1079 (2007).
[11] D. J. C. MacKay, *Information Theory, Inference, and Learning Algorithms* (Cambridge University Press, Cambridge, U.K., 2003).
[12] C. Chassin *et al.*, Am. J. Pathol. Renal Physiol. **293**, F927 (2007).
[13] L. Petit *et al.*, J. Biol. Chem. **276**, 15736 (2001).
[14] S. Miyata *et al.*, J. Biol. Chem. **277**, 39463 (2002).
[15] D. Casanova *et al.*, J. Am. Chem. Soc. **129**, 12592 (2007).
[16] E. Beaurepaire *et al.*, Nano Lett. **4**, 2079 (2004).
[17] D. Casanova *et al.*, Appl. Phys. Lett. **89**, 253103 (2006).
[18] V. Buissette *et al.*, J. Mater. Chem. **16**, 529 (2006).
[19] K. Ritchie *et al.*, Biophys. J. **88**, 2266 (2005).
[20] N. Destainville and L. Salomé, Biophys. J. **90**, L17 (2006).
[21] M. Smoluchowski, Ann. Phys. (Leipzig) **326**, 756 (1906).
[22] K. Suzuki *et al.*, Biophys. J. **79**, 448 (2000).
[23] H. Risken, *The Fokker-Planck Equation: Methods of Solutions and Applications* (Springer, New York, 1989).
[24] H. Kleinert, *Path integrals in Quantum Mechanics, Statistics, Polymer Physics and Financial Markets* (World Scientific, Singapore, 2006).
[25] See EPAPS Document No. E-PRLTAO-102-083906 for a movie at real speed. For more information on EPAPS, see http://www.aip.org/pubservs/epaps.html.